Springer

Acta Mechanica Sinica

CrossMark click for updates

• Research Paper •

Acta Mech. Sin., Vol. 41, 524931 (2025)
https://doi.org/10.1007/s10409-025-24931-x

Deep learning technique based efficient optimization method for cone dielectric energy generator

Demin Zhao[1*], Aoyu Xiao[1], Zewen Gu[1], Menghang Chen[1], Guoqiang Xu[1], Bin Zhao[2], and Jianlin Liu[1]

[1] *College of Pipeline and Civil Engineering, China University of Petroleum (East China), Qingdao 266580, China;*
[2] *Institute of Power Transmission and Transformation Engineering Technology, State Grid Electric Power Engineering Research Institute Co., Ltd, Beijing 100055, China*

Received December 18, 2024; accepted June 30, 2025; published online October 28, 2025

Dielectric elastomer (DE) is an electroactive polymer with the characteristics of high energy output, great flexibility, lightweight, mechanical compliance, and low cost, which are particularly suitable for DE energy generators. Energy harvesting efficiency is a key index to evaluate the performance of the energy generator, which depends on the structural configuration and the mechanical and dielectric properties of the DE material. This paper proposes a fractional viscoelastic polarization (FVP) model by combining the fractional viscoelasticity model and the polarization-based lumped parameter model. A dynamical model of a cone dielectric energy generator (CDEG) considering stretch-dependent electrostriction and nonlinear viscoelasticity is established. Additionally, a deep neural network (DNN) model is developed to explore the relationships between various parameters and the output energy of CDEGs to efficiently and accurately predict the energy output of CDEGs. Based on the DNN model, optimal parameter designs for CDEGs are obtained by using non-dominated sorting genetic algorithm II (NSGA-II). The experiments verified that the FVP model predicts accurately the output energy of CDEG and the established optimal design framework can accurately provide the optimal design parameters of CDEG, which offers deep insights for the design and fabrication of a high-efficiency dielectric energy generator.

Cone dielectric energy generator, Energy harvesting, Fractional viscoelasticity, Stretch-dependent electrostriction, Deep neural network

Citation: D. Zhao, A. Xiao, Z. Gu, M. Chen, G. Xu, B. Zhao, and J. Liu, Deep learning technique based efficient optimization method for cone dielectric energy generator, Acta Mech. Sin. 41, 524931 (2025), https://doi.org/10.1007/s10409-025-24931-x

1. Introduction

With the development of society, the demand for energy has surged. It is imperative to explore efficient methods for harnessing ambient energy. Generally, the available energy sources in the environment encompass mechanical, solar, thermal, electromagnetic, and chemical energies [1]. Among these, mechanical energy garners particular attention due to its wide distribution. As vibration is a significant form of mechanical energy, vibration energy generator possesses a multitude of potential application areas, including wave energy harvesting [2,3], energy collection from human motion [4,5], energy capture from vehicle and road vibrations [6-8], as well as harvesting energy from structural vibrations [9], and so on. The development of highly efficient devices to harvest environmental vibration energy is of paramount importance for modern energy advancement. In recent decades, numerous novel energy harvesting methods have been developed, including dielectric elastomer generators (DEGs) [10,11], triboelectric nanogenerators [12], and piezoelectric generators [13]. Among these, DEGs have gained significant attention due to their advantages, including low cost, lightweight, ease of manufacturing, and high energy density [14-17], thereby attracting substantial research efforts aimed at developing high-performance energy harvesting devices.

*Corresponding author. E-mail address: zhaodemin@upc.edu.cn (Demin Zhao)
Executive Editor: Rui Huang

The conversion of mechanical energy into electrical energy of DEGs is achieved through the capacitive changes that occur during the deformation process of the dielectric elastomer (DE). DEs have a high energy density, reaching up to 400 mJ/g under ideal conditions. This indicates that each gram of DE material is capable of delivering 400 mJ of electrical energy per cycle [18]. Therefore, a significant number of dielectric energy generators have already been developed for various fields. For instance, Du et al. [3,11] proposed a series of DEG for a wave energy generator with output of 60 mW and 1.75 W. In the field of wind energy harvesting, a set of DE vibrational wind energy generators are studied by Lai et al. [19], achieving an output ranging from 0.16 and 0.7125 mW [20]. Ichikawa and Hijikata [5] developed a thin sheet DEG of bite force energy, producing an output of 2.5 μW under bite loads. Xie et al. [21] proposed an alternative current DEG for harvesting energy from the joint movements of human beings.

Although DEGs have been fully developed in various application scenarios, the constitutive modeling of DE is a core challenge due to the finite deformation of the soft DE materials. The majority of studies still primarily consider the assumptions of hyperelasticity constitutive modeling and standard Maxwell stress in DE [11,22,23]. However, many studies indicate that DE exhibits complex material characteristics, such as nonlinear viscoelasticity [24], viscoplasticity [25,26], and electrostriction [27,28]. For considering the viscoelasticity of DEs, integer-order viscoelasticity models are commonly employed, typically incorporating internal variables to describe energy dissipation during the deformation process, which often introduce multiple control parameters [29-31]. Fortunately, fractional viscoelasticity models have recently been developed for DE materials, which need much fewer internal variables and governing equations than integer-order viscoelasticity models, and hence attract the interest of researchers [32,33]. Moreover, DE materials exhibit intricate electromechanical coupling phenomena. Experimental evidence indicates that the influence of deformation state on the dielectric constant of DEs, i.e., stretch-dependent electrostriction, is substantial and cannot be disregarded [34,35]. Until now, several models have been developed to characterize the stretch-dependent electrostriction [27,35-37]. Kumar and Patra [38] evaluated five types of stretch-dependent electrostriction models and concluded that the polarization-based lumped parameter model exhibited the best fit [37]. The highly nonlinear material properties of DEs can significantly affect the performance of DE devices [39], so further consideration of these properties is required in the research of DEGs.

In addition to the material properties of DE, various other factors also affect the energy harvesting efficiency of DEG systems, including geometric dimensions, characteristics of external voltage input, and so on. Analyzing the synergistic influence of multiple parameters and finding optimal design parameters are significant challenges in DEG design and optimization. Most of the in-depth investigations of these problems were conducted using "one-factor-at-a-time" technique, which only investigates the effects of a design variable on responses of the design goal, and applying optimal method on complex theory and numeral model, rather than evaluating the interactive effects of all relevant variables on the overall performance to identify optimal design in whole design domain. For example, Haroun and Lee [40] employed several simulations of different DEG's parameters to analysis on the charging performance of the DE-triboelectric generator and optimize their performance. Jiang et al. [41] developed a pre-stretch control method and optimized the design dimensions and operational distance of conical DEGs through experimental studies and then achieved an energy output density of 130 mJ/g and a conversion efficiency of up to 40%. However, considering the nonlinear viscoelasticity and electrostriction of DE, along with the complex characteristics introduced by structural design, the interactions among various parameters of DEG are complex and unstable. Conventional methods have difficulties in implementation, and more effective research methods are needed.

These works mentioned above contribute significantly to the development of DEGs. Recent research has begun to employ machine learning to study DE devices [42]. Wang et al. [43] employed a topology optimization method based on genetic algorithms to design the optimal electrode configuration for dielectric elastomer actuators (DEAs). Ma et al. [44] combined finite element methods, deep neural networks (DNNs), and particle swarm optimization to accurately predict the deformation of DE beams. Li et al. [45] proposed a data-driven framework for long-term energy consumption prediction of DEAs. These studies demonstrate that machine learning method can handle more complex problems compared to traditional optimization design methods.

Enhancing the accuracy of performance prediction for DEG can be significantly achieved by considering the nonlinear viscoelasticity and electrostriction. However, the design and analysis of DEG are challenged by the highly complex effects of both the nonlinear material properties of DE and the intricate structural parameters of DEG. Nevertheless, the machine learning method is adept at efficiently capturing these multi-parameter complex relationships to facilitate rapid and precise prediction and analysis of DEG. The combination of the DEG model with nonlinear viscoelasticity, stretch-dependent electrostriction, and machine learning methods can achieve fast and accurate design and optimization of DEG.

In this study, a fractional viscoelastic polarization (FVP) model is proposed to establish the dynamic model, and the energy harvesting theory of the cone dielectric energy generator (CDEG) is presented in Sect. 2. The dynamic model and energy harvest theory are verified in Sect. 3. In Sect. 4, through DNNs, the relationship between design

parameters and the output energy of CDEG is established. Additionally, the non-dominated sorting genetic algorithm II (NSGA-II) method is employed to investigate the optimal energy output design of the CDEG in a low-frequency working environment, and experimental validation is conducted for the optimized results in Sect. 5. Finally, Sect. 6 concludes this work.

2. Theoretical model

In this section, the CDEG is introduced, followed by a comprehensive explanation of its operational mechanism. The polarization-based lumped parameter model and the fractional viscoelasticity model are integrated to characterize the electrostriction and viscoelasticity of CDEGs. Subsequently, the dynamic equation of the CDEG is established using the generalized Hamiltonian principle. Finally, the energy harvesting theory is presented.

2.1 Physical model

In this paper, the schematic of CDEG is illustrated in Fig. 1. The conical structure comprises a pre-stretched DE circular film and two sets of rigid frames. An annular rigid structure with an inner radius r_b supports the DE film, which has undergone biaxial pre-stretching, characterized by a pre-stretch ratio λ_p. Additionally, two rigid blocks, with a radius r_a, are affixed at the center of the circular film. The DE film forms a circular truncated cone structure, supported by a linear spring with a stiffness k_s. Flexible electrodes are pasted on both sides of the DE film. By intermittently applying voltage and suitable external forces, the CDEG can achieve efficient energy harvesting.

In reality, the generatrix of the cone structure is curved, but without sacrificing accuracy, we consider it as a straight line. We assume the film remains homogeneous during deformation, with only the film on the sides of the cone involved in the deformation. Additionally, the spring is regarded as an ideal linear spring. The entire system is treated as a single degree of freedom dynamic system. The global coordinate system x-O-y is illustrated in Fig. 1, where the original length of the spring is denoted by h, and the position of the rigid block from the origin is defined as x. External excitation is applied on the top of the rigid block, causing it to move in the direction of the x-axis, thus driving the film to elongate or contract.

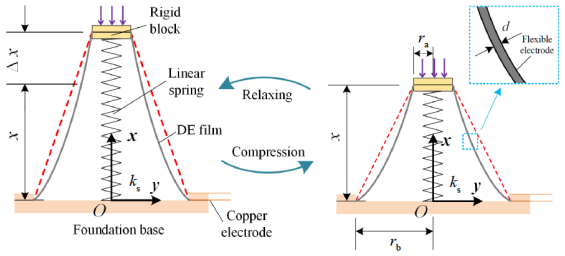

Figure 1 Structural schematic of CDEG.

2.2 FVP model

The FVP model is presented by integrating the fractional viscoelasticity model with a polarization-based lumped parameter model. The standard viscoelasticity model is depicted in Fig. 2(a). Then, the series connection of spring and dashpot is replaced by a fractional spring-pot element, and the parallel spring is substituted by another spring element with a lumped parameter model based on polarization. Thus, the FVP model is obtained as illustrated in Fig. 2(b). Here, E_1 and E_2 represent the elastic moduli, C_i denotes the purely elastic parameters, c_i represents the pure electrical parameters and the electromechanical coupling parameters, η is the viscosity coefficient of the fractional viscoelasticity model, and α indicates the order of the fractional derivative.

The polarization-based lumped parameter model is based upon the stretch dependence of polarization within dielectric materials, which is similar to the constitutive expression of fiber-reinforced material [37,46]. Therefore, the free energy function of DE with a function of six invariants can be written as

$$w = w(I_1, I_2, I_3, I_4, I_5, I_6), \tag{1}$$

where individual invariants are shown as follows [46]:

$$\begin{aligned} I_1 &= \mathrm{tr}(\mathbf{C}), & I_2 &= \frac{1}{2}[\mathrm{tr}^2(\mathbf{C}) - \mathrm{tr}(\mathbf{C}^2)], \\ I_3 &= \det(\mathbf{C}), & I_4 &= \widetilde{\mathbf{E}} \cdot \widetilde{\mathbf{E}}, \\ I_5 &= \widetilde{\mathbf{E}} \cdot \mathbf{C}^{-1} \cdot \widetilde{\mathbf{E}}, & I_6 &= \widetilde{\mathbf{E}} \cdot \mathbf{C}^{-2} \cdot \widetilde{\mathbf{E}}, \end{aligned} \tag{2}$$

where $\mathbf{C}$ is the right Cauchy-Green tensor, denoted by $\mathbf{C} = \mathbf{F}^{\mathrm{T}}\mathbf{F}$, $\mathbf{F}$ is the deformation gradient tensor, the reference electric field $\widetilde{\mathbf{E}}$ and the spatial electric field $\mathbf{E}$ are linked via $\widetilde{\mathbf{E}} = \mathbf{F}^{\mathrm{T}}\mathbf{E}$; the invariants I_1, I_2, and I_3 are only related to mechanical deformation; I_4 characterizes the contribution of pure electricity; I_5 and I_6 contain mechanical and electrical parameters that characterize the contribution of electromechanical coupling. The free energy function w can be divided into w_h and w_e, which are induced by pure de-

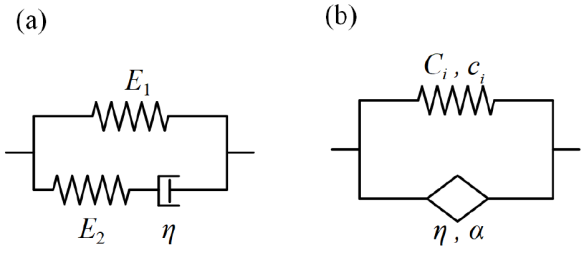

Figure 2 Viscoelasticity models for DE: (a) standard viscoelasticity solid model; (b) FVP model.

formation and electric field, respectively. To further simplify the model, the components of the free energy function w_e are assumed to be a linear function of electric invariants. And we select the Yeoh model to represent w_h as it exhibits outstanding predictive accuracy for the electromechanical behavior of VHB4910, the material utilized in this research [47]. The free energy expression w and its components w_h and w_e are written as

$$w = w_h(I_1, I_2, I_3) + w_e(I_4, I_5, I_6), \tag{3}$$

$$w_h = C_1(I_1-3) + C_2(I_1-3)^2 + C_3(I_1-3)^3 - p(J-1), \tag{4}$$

$$w_e = c_1 I_4 + c_2 I_5 + c_3 I_6, \tag{5}$$

where C_1, C_2, and C_3 are material parameters of the Yeoh model, p is the hydrostatic pressure, J is the determinant of $\mathbf{F}$, and c_1, c_2, and c_3 are material parameters of the electric part. The parameters C_i and c_i (i = 1, 2, 3) all need to be determined by experiment.

Characterizing the viscoelasticity and electrostriction of DE material, the FVP model is adopted as shown in Fig. 2(b). For this model, the total Cauchy stress can be simply obtained by summing the stress of a hyperelastic spring and a fractional spring-pot. We employ a polarization-based lumped parameter model as the hyperelastic component of the FVP model. The total Cauchy stress can be written as

$$\boldsymbol{\sigma}_{\text{total}} = \boldsymbol{\sigma}_s + \boldsymbol{\sigma}_v. \tag{6}$$

The stress $\boldsymbol{\sigma}_s$ is hyperelastic stress obtained from the polarization-based lumped parameter model [37] as follows:

$$\boldsymbol{\sigma}_s = \mathbf{F}\frac{\partial w_h}{\partial \mathbf{F}}\mathbf{F}^{\mathrm{T}} + \mathbf{F}\frac{\partial w_e}{\partial \mathbf{F}}\mathbf{F}^{\mathrm{T}} = \boldsymbol{\sigma}_h + \boldsymbol{\sigma}_e, \tag{7}$$

where $\boldsymbol{\sigma}_h$ represents the hyperelastic stress induced by pure mechanical deformation, and $\boldsymbol{\sigma}_e$ denotes the hyperelastic stress generated by the applied electric field and the electromechanical coupling.

The viscosity stress of the spring-pot is given by [48]

$$\boldsymbol{\sigma}_v = 2\eta \mathbf{D}^{\{\alpha\}}, \tag{8}$$

where $\mathbf{D}^{\{\alpha\}}$ is the fractional derivative of the rate of deformation tensor and $\mathbf{D} = \frac{1}{2}\left[\dot{\mathbf{F}}\mathbf{F}^{-1} + \mathbf{F}^{-\mathrm{T}}\dot{\mathbf{F}}^{\mathrm{T}}\right]$. Then, $\mathbf{D}^{\{\alpha\}}$ can be expressed in detail as

$$\mathbf{D}^{\{\alpha\}} = \frac{1}{\Gamma(1-\alpha)}\int_0^t (t-\tau)^{-\alpha}\mathbf{F}^{-\mathrm{T}}(\tau)\cdot\mathbf{F}^{\mathrm{T}}(t)\cdot\mathbf{D}(\tau) \cdot\mathbf{F}(t)\cdot\mathbf{F}^{-1}(\tau)\mathrm{d}\tau, \tag{9}$$

where $\Gamma(*)$ is the Euler-gamma function, whose definition is $\Gamma(t) = \int_0^\infty t^{t-1}\exp(-\tau)\mathrm{d}\tau$.

Substituting Eqs. (7) and (8) into Eq. (6), a FVP model of DE is derived. The expression of the total Cauchy stress is given by

$$\boldsymbol{\sigma}_{\text{total}} = \mathbf{F}\frac{\partial w_h}{\partial \mathbf{F}}\mathbf{F}^{\mathrm{T}} + \mathbf{F}\frac{\partial w_e}{\partial \mathbf{F}}\mathbf{F}^{\mathrm{T}} + 2\eta\mathbf{D}^{\{\alpha\}}. \tag{10}$$

The parameters (C_i, c_i, α, η, i = 1, 2, 3) of the FVP model are identified by experiments, as detailed in Appendix A.

2.3 Dynamic governing equation

The generalized Hamilton principle is used to establish the dynamic equation of CDEG by analyzing the kinetic energy, potential energy, viscous dissipative work, and external work of the system. The expression is as follows:

$$\int_{t_0}^{t_1}(\delta T - \delta V + \delta W)\mathrm{d}t = 0, \tag{11}$$

where δT is the kinetic energy variation, δV is the potential energy variation, δW is the virtual work of the external and dissipative forces, and $[t_0, t_1]$ represent any fixed time interval.

The kinetic energy of the system is composed of the kinetic energy of the rigid blocks, spring, and flexible film. By integrating the solid domain, the total kinetic energy can be written as follows:

$$T = \frac{1}{2}m_0\dot{x}^2 + \iiint_{\Omega}\frac{1}{2}\rho_0 v^2\mathrm{d}\Omega, \tag{12}$$

where m_0 is the equivalent mass of components except the film, including the mass of rigid blocks and the equivalent mass of springs. ρ_0 is the DE film density, Ω is the current spatial area occupied by DE film, and v is the velocity of a mass point at any position on the film in the current coordinate system. Due to the assumption of uniform deformation, each mass point velocity of the membrane is denoted by

$$v = \frac{(r_b - y)}{r_b - r_a}\dot{x}. \tag{13}$$

The velocity direction is forward along the x-axis. Substituting Eq. (13) into Eq. (12), the kinetic energy expression can be written as

$$T = \frac{1}{2}m_0\dot{x}^2 + \pi\rho_0 d_0\lambda_p^{-2}\dot{x}^2 \cdot\left[\frac{r_b^2\left(r_b^2 - r_a^2\right)}{2(r_b - r_a)^2} - \frac{2}{3}r_b\frac{\left(r_b^3 - r_a^3\right)}{(r_b - r_a)^2} + \frac{1}{4}\left(r_b^2 + r_a^2\right)\right], \tag{14}$$

where d_0 is the initial thickness of the DE membrane. Let $r = r_b - r_a$, the variation of Eq. (14) be rewritten as

$$\delta T = m_0\dot{x}\delta\dot{x} + V_0\rho_0 \cdot\left[\frac{r_b^2}{2r^2} - \frac{2}{3}r_b\frac{\left(r_b^3 - r_a^3\right)}{r^2\left(r_b^2 - r_a^2\right)} + \frac{1}{4}\frac{\left(r_b^2 + r_a^2\right)}{\left(r_b^2 - r_a^2\right)}\right]\dot{x}\delta\dot{x}, \tag{15}$$

where V_0 denotes the volume of the DE membrane. By using integration by parts, the integral form of Eq. (11) can be rewritten as

$$\int_{t_0}^{t_1}\delta T\mathrm{d}t=\int_{t_0}^{t_1}\left\{-m_0\ddot{x}\delta x-V_0\rho_0\left[\frac{r_\mathrm{b}^2}{2r^2}-\frac{2}{3}r_\mathrm{b}\cdot\frac{\left(r_\mathrm{b}^3-r_\mathrm{a}^3\right)}{r^2\left(r_\mathrm{b}^2-r_\mathrm{a}^2\right)}+\frac{1}{4}\frac{\left(r_\mathrm{b}^2+r_\mathrm{a}^2\right)}{\left(r_\mathrm{b}^2-r_\mathrm{a}^2\right)}\right]\ddot{x}\delta x\right\}\mathrm{d}t. \tag{16}$$

The potential energy V contains elastomer strain energy, electric potential energy, and linear spring potential energy, which can be expressed as

$$V=\iiint_\Omega w\mathrm{d}\Omega+\frac{1}{2}k_\mathrm{s}(x-h)^2, \tag{17}$$

where w is the free energy density of the DE film, denoted by Eq. (3), and k_s is the stiffness of the linear spring.

Since the reference electric field $\widetilde{\mathbf{E}}$ is along the thickness direction of the DE film, we assume $\widetilde{\mathbf{E}}$ = [0, 0, e_0]. Substitute Eqs. (3)-(5) into Eq. (17), and the existing relation is given by $\lambda_1=\lambda_\mathrm{p}\sqrt{x^2+r^2}/r,\lambda_2=\lambda_\mathrm{p},\lambda_3=\lambda_1^{-1}\lambda_2^{-1}$, $I_1=\lambda_1^2+\lambda_2^2+\lambda_1^{-2}\lambda_2^{-2}$, $I_2=\lambda_1^2\lambda_2^2+\lambda_1^{-2}+\lambda_2^{-2}$, $J=\sqrt{I_3}=1$, $I_4=e_0^2$, $I_5=\lambda_3^{-2}e_0^2$, and $I_6=\lambda_3^{-4}e_0^2$. Here, λ_1-λ_3 are the stretch ratios along the generatrix, circumferential, and thickness directions of the conical film, respectively. Then, the detailed expression of potential energy is obtained as

$$\begin{aligned}V=&\frac{1}{2}k_\mathrm{s}(x-h)^2+V_0\left\{C_1\left(\lambda_\mathrm{p}^2\frac{x^2+r^2}{r^2}+\lambda_\mathrm{p}^2+\lambda_\mathrm{p}^{-4}\frac{r^2}{x^2+r^2}-3\right)+C_2\left(\lambda_\mathrm{p}^2\frac{x^2+r^2}{r^2}+\lambda_\mathrm{p}^2+\lambda_\mathrm{p}^{-4}\frac{r^2}{x^2+r^2}-3\right)^2+C_3\right.\\&\left.\cdot\left(\lambda_\mathrm{p}^2\frac{x^2+r^2}{r^2}+\lambda_\mathrm{p}^2+\lambda_\mathrm{p}^{-4}\frac{r^2}{x^2+r^2}-3\right)^3+a_1e_0^2+a_2\lambda_\mathrm{p}^2\cdot\frac{x^2+r^2}{r^2}e_0^2+a_3\lambda_\mathrm{p}^4\frac{(x^2+r^2)^2}{r^4}e_0^2\right\}.\end{aligned} \tag{18}$$

The electric intensity e_0 can be calculated using input voltage U_in and initial DE film thickness d_0, $e_0=U_\mathrm{in}/d_0$. The variational form of potential energy with respect to the generalized coordinate x can be expressed by

$$\begin{aligned}\delta V=&k_\mathrm{s}(x-h)\delta x+V_0\left\{C_1\left[\lambda_\mathrm{p}^2\frac{2x\delta x}{r^2}-\frac{2r^2x\delta x}{\lambda_\mathrm{p}^4(x^2+r^2)^2}\right]\right.\\&+2C_2(I_1-3)\left[\lambda_\mathrm{p}^2\frac{2x\delta x}{r^2}-\frac{2r^2x\delta x}{\lambda_\mathrm{p}^4(x^2+r^2)^2}\right]\\&+3C_3(I_1-3)^2\left[\lambda_\mathrm{p}^2\frac{2x\delta x}{r^2}-\frac{2r^2x\delta x}{\lambda_\mathrm{p}^4(x^2+r^2)^2}\right]\\&\left.+a_2\frac{2\lambda_\mathrm{p}^2x\delta x}{R^2}\left(\frac{U_\mathrm{in}}{d_0}\right)^2+a_3\frac{4\lambda_\mathrm{p}^4x(x^2+r^2)\delta x}{R^4}\left(\frac{U_\mathrm{in}}{d_0}\right)^2\right\}.\end{aligned} \tag{19}$$

The total external virtual work δW includes external force virtual work δW_f and viscous dissipative virtual work δW_v. δW can be written as

$$\delta W=\delta W_\mathrm{f}+\delta W_\mathrm{v}=F\delta x-c\dot{x}\delta x+\iiint_{\Omega_0}\mathbf{s}_\mathrm{v}:\delta\mathbf{F}\mathrm{d}\Omega_0, \tag{20}$$

where c represents the structural damping of the structure without DE film, F denotes the external force, and $\mathbf{s}_\mathrm{v}$ is the viscosity nominal stress tensor. The viscosity stress $\boldsymbol{\sigma}_\mathrm{v}$ is provided by Eqs. (8) and (9), and further, it can be written as

$$\begin{aligned}\mathbf{s}_\mathrm{v}=&\mathbf{F}^{-1}\boldsymbol{\sigma}_\mathrm{v}=2\eta\mathbf{F}^{-1}\mathbf{D}^{\{\alpha\}}\\=&\frac{2\eta}{\Gamma(1-\alpha)}\int_0^t(t-\tau)^{-\alpha}\left[\lambda_1(t)\lambda_1^{-3}(\tau)\cdot\dot{\lambda}_1(\tau)\mathbf{e}_1\otimes\mathbf{e}_1+0\mathbf{e}_2\otimes\mathbf{e}_2\right.\\&\left.-\lambda_1^{-1}(t)\lambda_p\lambda_1(\tau)\dot{\lambda}_1(\tau)\mathbf{e}_3\otimes\mathbf{e}_3\right]\mathrm{d}\tau,\end{aligned} \tag{21}$$

where $\mathbf{e}_1$ represents the unit base vector in the direction of the cone's generatrix, $\mathbf{e}_2$ is the circumferential unit base vector, and $\mathbf{e}_3$ is the unit base vector in the direction of the film's thickness.

Substituting Eq. (21) into Eq. (20), the external virtual work can be rewritten as

$$\delta W=-c\dot{x}\delta x+F(t)\delta x+V_0\left[-\eta\lambda_\mathrm{p}^2\frac{x}{r^2}D_1^{\{\alpha\}}+\eta\lambda_\mathrm{p}^{-2}\cdot\frac{r^2x}{(x^2+r^2)^2}D_2^{\{\alpha\}}\right]\delta x, \tag{22}$$

where the fractional operators are expressed as

$$\begin{aligned}D_1^{\{\alpha\}}=&-\frac{2}{\Gamma(1-\alpha)}\int_0^t(t-\tau)^{-\alpha}\lambda_1^{-3}(\tau)\dot{\lambda}_1(\tau)\mathrm{d}\tau,\\D_2^{\{\alpha\}}=&\frac{2}{\Gamma(1-\alpha)}\int_0^t(t-\tau)^{-\alpha}\lambda_1(\tau)\dot{\lambda}_1(\tau)\mathrm{d}\tau.\end{aligned} \tag{23}$$

Substituting Eqs. (16), (19), and (22) into Eq. (11), according to the variational principle, the dynamic equation of the proposed model is derived as

$$m_\mathrm{r}\ddot{x}+f_\mathrm{m}\ddot{x}+k_\mathrm{s}(x-h)+c\dot{x}+f_\mathrm{c}=F(t)+f_\mathrm{v}(x,t), \tag{24}$$

where

$$m_\mathrm{r}=m_0+V_0\rho_0\left[\frac{r_\mathrm{b}^2}{2r^2}-\frac{2}{3}r_\mathrm{b}\frac{\left(r_\mathrm{b}^3-r_\mathrm{a}^3\right)}{r^2\left(r_\mathrm{b}^2-r_\mathrm{a}^2\right)}+\frac{1}{4}\frac{\left(r_\mathrm{b}^2+r_\mathrm{a}^2\right)}{\left(r_\mathrm{b}^2-r_\mathrm{a}^2\right)}\right],$$

$$f_\mathrm{m}=V_0\rho_0\left[\frac{r_\mathrm{b}^2}{2r^2}-\frac{2}{3}r_\mathrm{b}\frac{\left(r_\mathrm{b}^3-r_\mathrm{a}^3\right)}{r^2\left(r_\mathrm{b}^2-r_\mathrm{a}^2\right)}+\frac{1}{4}\frac{\left(r_\mathrm{b}^2+r_\mathrm{a}^2\right)}{\left(r_\mathrm{b}^2-r_\mathrm{a}^2\right)}\right],$$

$$\begin{aligned}f_\mathrm{c}=&V_0\left\{C_1\left[\frac{2x}{R^2}-\frac{2R^2x}{\lambda_\mathrm{p}^2(x^2+r^2)^2}\right]+2C_2(I_1-3)\left[\lambda_\mathrm{p}^2\frac{2x}{r^2}-\frac{2r^2x}{\lambda_\mathrm{p}^4(x^2+r^2)^2}\right]\right.\\&\left.+3C_3(I_1-3)^2\left[\lambda_\mathrm{p}^2\frac{2x}{r^2}-\frac{2r^2x}{\lambda_\mathrm{p}^4(x^2+r^2)^2}\right]+a_2\frac{2\lambda_\mathrm{p}^2x}{R^2}\left(\frac{U_\mathrm{in}}{d_0}\right)^2+a_3\frac{4\lambda_\mathrm{p}^4x(x^2+r^2)}{R^4}\left(\frac{U_\mathrm{in}}{d_0}\right)^2\right\},\end{aligned}$$

$$f_{\mathrm{v}} = V_0\left[\eta\lambda_{\mathrm{p}}^{2}\frac{x}{r^2}D_1^{\{\alpha\}} - \eta\lambda_{\mathrm{p}}^{-2}\frac{r^2 x}{(x^2+r^2)^2}D_2^{\{\alpha\}}\right].$$

Due to the highly nonlinearity of the dynamic equations incorporating fractional-order components, the modified fourth-order Runge-Kutta method is adopted to numerically solve the equations referenced to Ref. [48].

2.4 Energy harvest theory

The energy harvesting theory of CDEG is described in detail in this sub-section. The entire process of energy harvesting comprises three states. As shown in Fig. 3, in State I, mechanical force stretches the DE film to increase its surface area, decrease its thickness, and increase its capacitance. The capacitance of CDEG can be calculated by $C = \varepsilon_0\varepsilon_r S/d$, where S is the area of CDEG covering the electrode, and d is the film thickness. The external power supply provides a charge to maintain a stable voltage. Then the charges on both sides of the DE film are increasing greatly. Subsequently, in State II, the DE membrane shrinks due to the combined effects of its own restoring force and external load when the power supply is disconnected. As a result, the DE film's thickness increases, surface area lessens, and capacitance decreases, indicating State II. The charge Q remains constant during this process, and the voltage on both sides of CDEG will increase, denoted as $U = Q/C$. Finally, in State III, the increased electric energy is transferred to an energy storage device or the electrical appliance, and the electrode voltage eventually returns to the initial state. It is worth noting that throughout the entire process, the power supply only provides a certain initial energy to maintain the potential difference across the DE film. If energy losses are not considered, the total energy released ultimately includes both the electrical energy provided by the power supply and the electrical energy converted by the DEG. Based on the working process cycle, mechanical energy can be continuously converted into electrical energy to achieve the purpose of efficient energy harvesting.

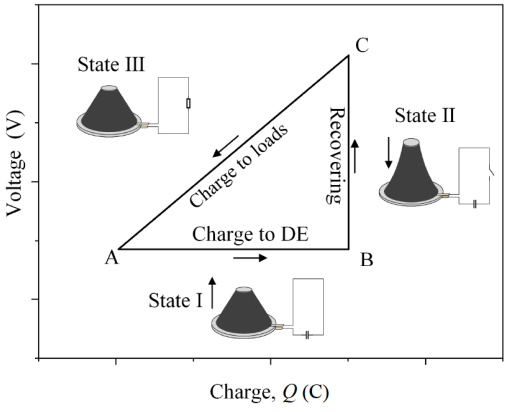

Figure 3 Voltage-charge plot of electric cycle.

Due to the capability of DE materials to generate charge independently and the inevitable charge loss in the circuit, an external power source is required to maintain the charge. To realize the operational principle, a circuit design that can stably guarantee the charge supply is needed. Moreover, an energy harvest loop is used to verify the generation of electric energy, as shown in Fig. 4(a). Part I represents the power supply circuit, which provides the power supply to furnish charge to supplement the charge loss in the right loop, and the diode prevents the charge from flowing back to the power supply when the voltage of the CDEG increases. Part II indicates the energy generation circuit. When the DE membrane shrinks, the capacitance of CDEG decreases, and the voltage rises. The voltage of CDEG exceeds the breakdown voltage of the diode, the diode turns on and supplies power to the load until the voltage drops, causing the diode to reactivate. Part III is the monitoring circuit. R1 is a high resistance resistor with a resistance value of 10^9-10^{10} Ω, R2 represents the equivalent resistance of the oscilloscope internal resistance and external resistance in parallel, and its resistance value is between 10^6-10^7 Ω. The oscilloscope monitors the voltage at both ends of the DEs in real time. Here, the high-resistance resistor R1 is used to reduce the energy loss of the monitoring loop, and the resistance voltage divider is used to protect the oscilloscope.

In order to verify the peak output voltage of CDEG, the diode and load in Part II are removed, and the voltage change of the DE film is measured, as illustrated in Fig. 4(b). Due to the unidirectional conduction of the diode, the

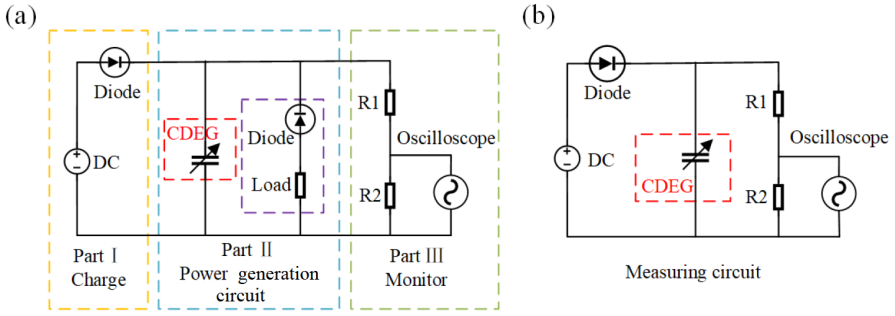

Figure 4 Circuit of energy harvesting: (a) energy harvesting circuit; (b) voltage monitoring circuit.

charge cannot flow back to the power supply during the cycle. The large resistance monitoring circuit reduces the charge loss to an acceptable range, and the minuscule amount of charge lost is compensated by the power supply. In this way, the power generation circuit can assume that the total amount of charge in the process is unchanged, and the maximum and minimum capacitance in the process of DE film deformation are defined as C_{max} and C_{min}, and the total constant electric charge can be expressed as $Q = C_{max}U_{in}$, where U_{in} is the input voltage. The voltage output value can be predicted by the change of the DE capacitor as follows:

$$U_{out} = \frac{C_{max}}{C_{min}}U_{in}. \tag{25}$$

Based on the obtained peak of output voltage, the energy harvesting efficiency of the device can be predicted. The input energy is equal to the energy stored in the DE capacitor (capacitor is C_{max} and voltage is U_{in}) when the CDEG is stretched at its maximum, and the output energy is the energy stored by C_{min} at the measured output voltage U_{out} after DE releases. Thus, the generated energy per circle ΔE, and the theoretical output power P_{out} can be written as

$$\Delta E = \frac{1}{2}C_{min}U_{out}^2 - \frac{1}{2}C_{max}U_{in}^2, \tag{26}$$

$$P_{out} = \Delta E \cdot f. \tag{27}$$

3. Experimental validation of the theoretical model

In this section, we implement two experiments. Firstly, the correctness and effectiveness of the theoretical model derived in Sect. 2 are validated by testing the dynamic response. Secondly, the output voltage and the electrical energy increase per cycle of the CDEG under different excitation frequencies are tested.

3.1 Setup of experiment

Prior to the dynamic test, the manufacturing process of CDEG involved in the experiment is demonstrated, as shown in Fig. 5. Initially, a circular DE film with an initial radius R_b is subjected to biaxial loading until the desired pre-stretch ratio λ_p is achieved. Consequently, the radius of the circular region transforms to r_b. Two circular rigid frames with radii r_a and r_b are employed to secure the boundary, thereby maintaining the pre-stretch ratio. Chemical 846 carbon conducting grease is adopted as the experimental flexible electrode, which is subsequently pasted to the surface of the dielectric film, and copper electrodes are connected to the flexible electrode. Then, a linear spring is used to further support the DE film to realize the out of plane stretching. Ultimately, the device is fixed to obtain an energy generator with a conical geometry.

The physical photograph of the test device is shown in Fig. 6. The apparatus is mounted in an inverted position on a rigid support structure. A high-voltage DC power supply and monitoring circuitry are connected to the apparatus, with an oscilloscope used to observe voltage fluctuations in the circuit during dynamic processes. An exciter with a digital signal generator and a digital signal amplifier to produce the required excitation signal is positioned beneath the apparatus. A force sensor is fixed to the impact head of the exciter to record the excited forces. Additionally, a laser displacement sensor is employed to monitor displacement changes resulting from deformation of the device.

Subsequently, we validate the dynamic phenomena and energy harvesting performance of the CDEG. In order to obtain accurate experimental parameters, we measure film thickness, geometric size of component, spring stiffness, original length of spring, component mass, and structural equivalent damping. Finally, the parameters used in experiments and numerical simulations are given in Table 1.

3.2 Validation of dynamical phenomena

Aimed at validating the dynamic equation Eq. (24), we carry out a vibration experiment as illustrated in Fig. 6 and compare the experiment results with the simulation results obtained by solving Eq. (24). CDEG with different pre-stretch ratios (λ_p = 2, 3) are fabricated. A high-voltage DC power supply maintains a constant voltage output of 1000 V, while other structural parameters are listed in Table 1. During our tests, the exciter applies sinusoidal excitation

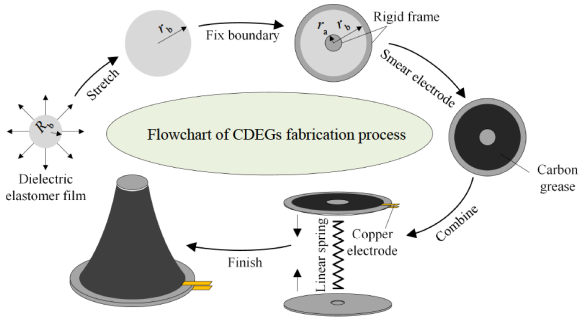

Figure 5 Manufacturing process of experimental device.

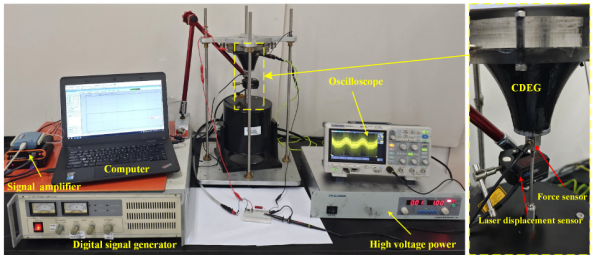

Figure 6 Physical device of CDEG and measuring circuit.

Table 1 Values of the parameters used in experiments and simulations

Structural parameters			Constitutive parameters		
Type of parameter	Parameter	Value	Type of parameter	Parameter	Value
Initial DE film thickness (m)	d_0	0.001	Yeoh coefficients (Pa)	C_1	14300
Base radius of the cone (m)	r_b	0.06		C_2	–520
Top radius of the cone (m)	r_a	0.0200		C_3	16
Original length of the spring (m)	h	0.1050	Lumped parameter model (F/m)	c_1	-1.3255×10^{-12}
Density of DE (kg/m^3)	ρ_0	960		c_2	-1.3884×10^{-11}
Structural damping (N·s/m)	c	2.0		c_3	6.1979×10^{-15}
Equivalent mass (kg)	m_r	0.0497	Fractional viscoelastic coefficient (Pa)	η	50000
Vacuum permittivity (F/m)	ε_0	8.8542×10^{-12}	Fractional derivative order	α	0.37
Spring stiffness (N/m)	k_s	600	–	–	–

forces with peak magnitudes of 1 N, and the frequencies are set as 1, 5, 10, 15, 20, 23, 25, 27, 30, 33, 35, 40, 45, and 50 Hz. The actual dynamic response of the CDEG is measured using laser displacement sensors. The amplitude-frequency response graphs of the simulation and experimental results are shown in Fig. 7. It is evident that both experimental and simulation results exhibit closely matching resonance peaks. Furthermore, time-domain comparisons of experimental and simulated data at several excited frequencies, as shown in Fig. 8, reveal that the proposed CDEG dynamical model effectively predicts the dynamic behavior.

3.3 Validation of harvesting performance

In order to evaluate the efficiency of the proposed FVP model for predicting the energy harvesting performance of CDEG. We carry out experiments to measure the capacitance, output voltage, and harvesting of electric energy per

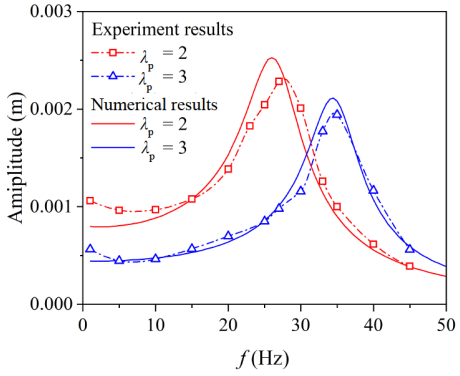

Figure 7 Comparison of frequency spectra between experimental and simulated data.

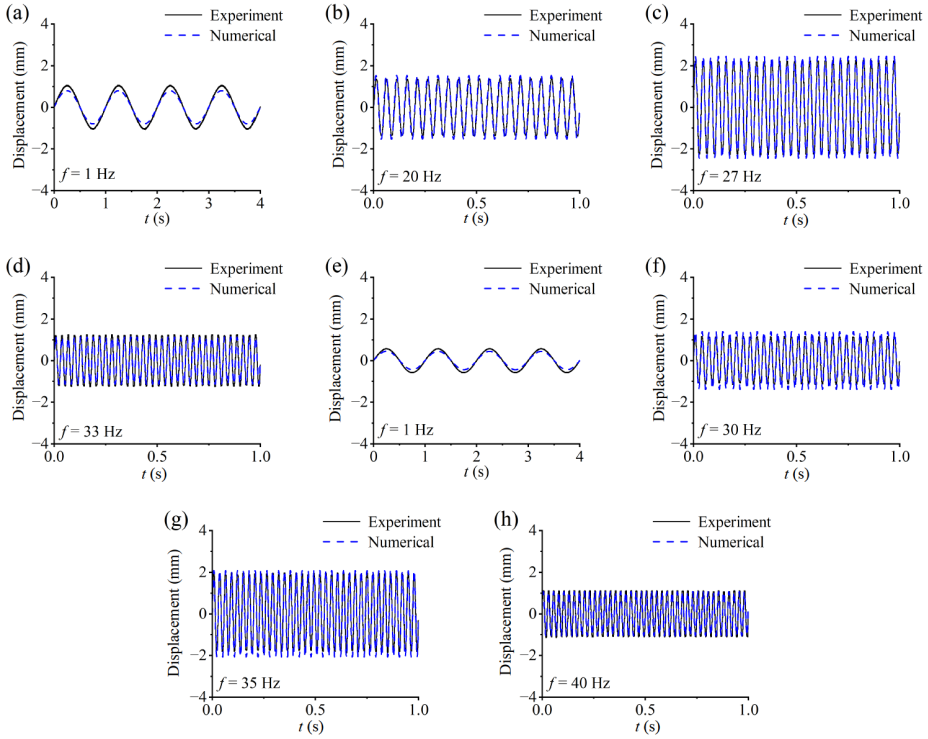

Figure 8 Comparing time-domain responses from experiment and simulation at critical frequencies: (a)-(d) pre-stretch ratio $\lambda_p = 2$; (e)-(h) pre-stretch ratio $\lambda_p = 3$.

cycle. We compare the test results with numerical results based upon the FVP model, considering stretch-dependent electrostriction and the general model (GM) with considering stretch-independent electrostriction. The GM model's parameters c_1 and c_3 in Eq. (5) related to the stretch ratio λ can be set to zeros, and the term c_2 can be set to 1.49×10^{-11} F/m.

Firstly, capacitance tests are conducted using CDEG with pre-stretch ratios of 1, 2, and 3, while keeping other parameters consistent with those listed in Table 1. The CDEG is compressed to change their cone height, and capacitance values are measured using a high-precision bridge meter at a frequency of 10 Hz for different heights. These experimental measurements are compared with the predicted values from both the FVP model and GM model, as illustrated in Fig. 9.

It can be found that as the pre-stretch ratio increases, the deviation between the GM model's numerical results and the experimental data becomes more pronounced. In contrast, the predictions of the FVP model align more closely with the experimental results. Therefore, the FVP model, considering stretch-dependent electrostriction, can more accurately predict the capacitance than the GM model, considering stretch-independent electrostriction.

In order to verify the efficiency of the proposed FVP model in energy harvesting efficiency prediction, the measurement circuit proposed in Sect. 2.4 is used to measure the output voltage of CDEG under different external excitation frequencies. We select CDEG with a pre-stretch ratio of 2 and test them under different input voltages of 1000, 1300, and 1500 V, as well as with external excitations of varying frequencies with a peak force of 1 N. The maximum output voltage is recorded for each condition. Additionally, the maximum voltages predicted by both the GM model and the FVP model are compared. The results are consistently presented in Fig. 10. It is observed that the predictions from both the GM and FVP models are the same close, with the GM model's predictions being slightly higher.

Furthermore, the energy generated by a single cycle of the CDEG operation is subsequently calculated, and these results are depicted in Fig. 11. It can be observed that as the input voltage increases, the energy output per cycle also increases correspondingly. The energy output predicted by the GM model exceeds the experimental results, while the FVP model provides predictions closer to the experimental results. This discrepancy is attributed to the FVP model's more accurate prediction of capacitance values, as shown in Fig. 9, which better agrees with actual conditions than the GM model.

In brief, based on the comparison between experimental data and theoretical predictions demonstrates that the CDEG dynamic system constructed using the FVP model has been validated, and the dielectric constant dependent on the deformation should be considered.

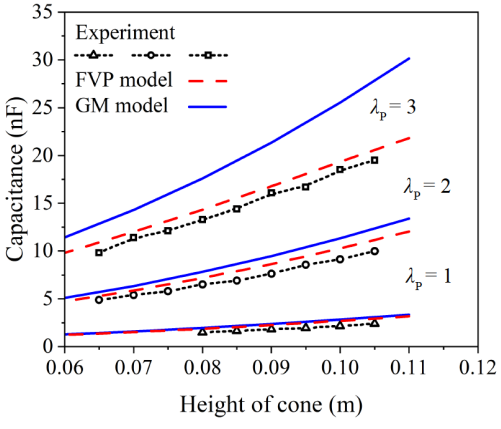

Figure 9 CDEG capacitance changes under different compression heights (including experimental and theoretical values).

4. Machine learning model for CDEGs

The analysis of the CDEG based FVP model includes solving the dynamic equation, implementing the iterative process, and calculating the ultimate outputs of the generated energy. The complicated process leads to significant computational costs for numerical solution, which also complicates the analysis of the synergistic effects between the multiple factors and the output energy. Machine learning techniques have revealed their robust abilities in tackling such problems as introduced in the literatures above. In this part, we employ DNNs to investigate the relationship between the output energy of the proposed model and multiple varying parameters. The synergistic effects of multiple CDEGs parameters on energy harvesting capacity are deeply analyzed through the developed DNN model.

4.1 Data preparation

The DNN model is a data-based model, which requires the selection of an appropriate dataset based on the specific question to ensure accurate training and testing. For effectively reflecting the attributes of the problem, the dataset

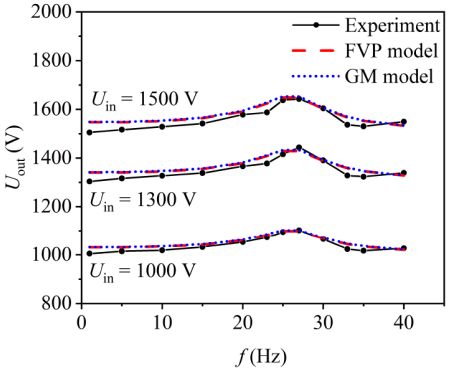

Figure 10 Output voltage of CDEG under different frequency excitations.

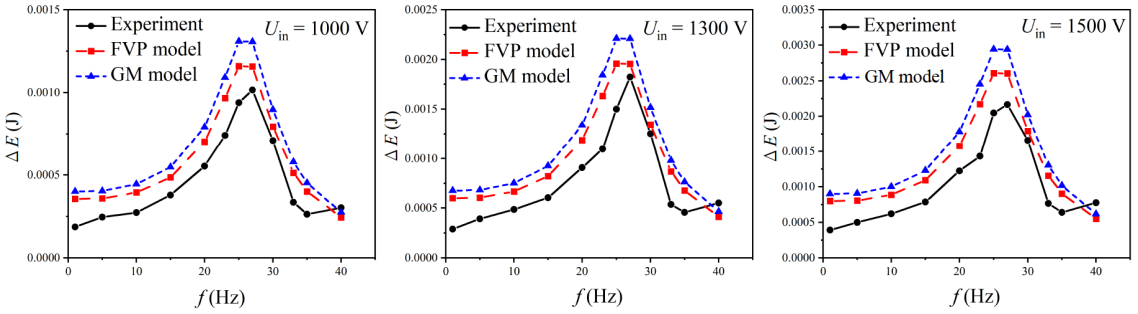

Figure 11 Electrical energy of CDEG varies with frequency in each cycle.

requires a sufficiently large number of data samples that are evenly distributed across the problem domain. Firstly, we employ Latin hypercube sampling techniques to establish an average-distributed set of parameters [49].

Six design parameters are defined as listed in Table 2, which are the input voltage U_{in}, pre-stretch ratio λ_p, excitation frequency f, excitation max force spring stiffness k_s, equivalent mass m_r, and the ratio of inner to outer diameter $\omega = r_a/r_b$, where $r_b = 0.06$ m, respectively. In experimental design, both the pre-stretch ratio λ_p and the input voltage V_{in} are limited to prevent mechanical rupture and electrical breakdown in the DE film. To ensure structural feasibility, the pre-stretch ratio range of 1 to 4 and an input voltage range of 1 to 3000 V is adopted. The spring stiffness k_s and equivalent mass m_r are selected based on experimental conditions. Specifically, the lower limit for spring stiffness is determined by the minimum stiffness k_s of available springs, and the minimum equivalent mass m_r is calculated after removing any additional mass from the system. Although k_s and m_r have no theoretical upper limit, they are capped at 3000 N/m and 0.5 kg for practicality. The excitation frequency range is chosen to encompass the entire resonance region, and the frequency range is set as 1 to 60 Hz based on both experimental observations and numerical simulations. The w is constrained by spring diameter and structural stability, set between 0.333 and 0.5. Based on the aforementioned results, the upper and lower bounds for each parameter are specified accordingly.

Based on the defined upper and lower bounds, a sample set of different variable combinations is generated using the Latin hypercube sampling techniques. The Latin hypercube sampling algorithm is coded in the commercial software MATLAB, resulting in a total of 2000 sampling points generated within the constrained domain. Subsequently, this dataset of parameters is used in the proposed theoretical model to solve the energy output results. Consequently, the dataset of 2000 sets of six structural attributes and their associated energy output parameters serves as the input for the development of the machine learning model.

Normalization ensures that different parameters are on the same scale, which is beneficial for enhancing the stability and generalization capability of the model. Hence, the min-max normalization method is employed, which transforms all parameters into the same range [0, 1]. The mathematical expression for this normalization technique is as follows:

$$y_{normal} = \frac{y_{real} - y_{min}}{y_{max} - y_{min}}, \tag{28}$$

where y_{normal} is the normalized value, y_{real} is the real value, and y_{min} and y_{max} are the minimum and maximum value of y_{real} in the whole data set.

In the training process of machine learning models, it is a common practice to split the training dataset into two parts: 75% training set and 25% testing set. Next, the 4-fold cross-validation method is utilized to assess the robustness of model training. As illustrated in Fig. 12, a random selection of 25% data samples from the entire dataset is designated as the test set, while the remaining samples are allocated to the training set. This process is repeated four times, resulting in four distinct data partitions for the validation set utilized in model training.

Table 2 Design parameters of CDEGs

Parameters	Lower bound	Upper bound	Symbol
Input voltage U_{in} (V)	0	3000	x_1
Pre-stretch ratio λ_p	1	4	x_2
Excitation frequency f (Hz)	1	60	x_3
Spring stiffness k_s (N/m)	45	3000	x_4
Equivalent mass m_r (kg)	0.02	0.5	x_5
The ratio of inner to outer radius ω	0.3333	0.5	x_6

4.2 DNN model for CDEGs

Deep neural networks are a type of artificial neural network (ANN) characterized by the presence of multiple hidden layers, in addition to input and output layers. The principle of the DNN is illustrated in Fig. 13. The data is initially fed into the input layer, where it undergoes modulation through activation functions within the hidden layers. Each hidden layer computes the weighted sum of the input parameters, representing the signal strength, which is then passed through an activation function and forwarded to the subsequent hidden layer. This process continues until the final output is generated at the output layer. DNN model is unable

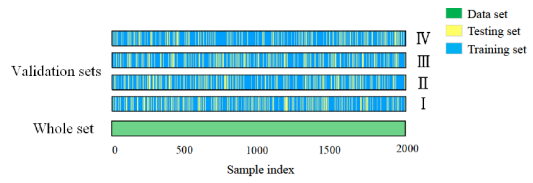

Figure 12 Partitioning of the testing and validation sets in 4-fold cross-validation.

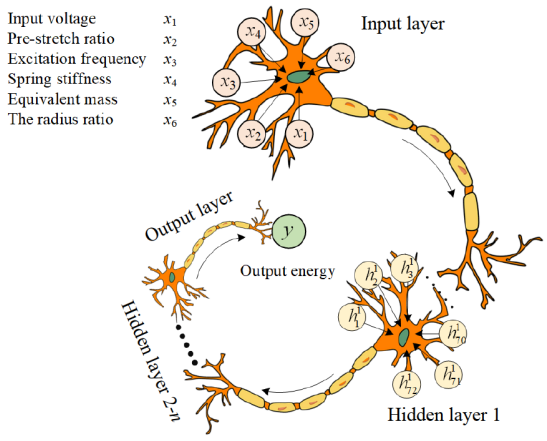

Figure 13 Operational principles of a deep ANN.

to describe the relationship between inputs and outputs using an explicit function. Instead, it captures the connection between them by constructing a complex hierarchical structure. As a result, DNN model is typically regarded as black box models, as it does not provide detailed insights into the internal structure of the model.

The DNN model is coded by using the Keras package in Python with TensorFlow as the backend. The network architecture is presented in Table 3. The adopted network consists of an input layer, an output layer, and six hidden layers. The number of nodes in the hidden layers is configured as 72, 72, 72, 72, 36, and 6, respectively. A total of 19132 parameters are included in the training process.

Figure 14 shows the training outcomes for the training set, with the data points generally aligning close to the validation line, which indicates that the training accuracy of the DNN model is at a high level. Simultaneously, the prediction results for the corresponding test set are also shown in Fig. 14, accompanied by the R^2 coefficients, which quantify the predictive performance relative to the actual outcomes. The R^2 coefficient is calculated by

$$R^2 = 1 - \frac{\sum_{i=1}^{n}(y_i - \hat{y}_i)^2}{\sum_{i=1}^{n}(y_i - \bar{y})^2}, \tag{29}$$

where y_i represents the value of the i^{th} test sample, $\hat{y}_i$ denotes the predicted value for the i^{th} sample, and $\bar{y}$ signifies the mean value of the test data, n represents the total number of test samples. Figure 14 presents the predictions for four validation sets, with R^2 of 0.9572, 0.9188, 0.9456, and 0.9307, respectively. These results indicate that the trained DNN model exhibits a high predictive capability for the energy output of CDEGs. Moreover, the choice of dataset does not significantly impact the model's accuracy. Subsequently, the DNN model corresponding to the optimal performance Group I is utilized as the final predictive model for subsequent parameter analysis and optimization processes.

Table 3 Structure of layers and elements in the DNN model

Layer	Output shape	Parameters
Input layer	(None, 6)	6
Hidden layer 01 (Dense)	(None, 72)	504
Hidden layer 01 (Dense)	(None, 72)	5256
Hidden layer 01 (Dense)	(None, 72)	5256
Hidden layer 01 (Dense)	(None, 72)	5256
Hidden layer 01 (Dense)	(None, 36)	2628
Hidden layer 01 (Dense)	(None, 6)	222
Output layer (Dense)	(None, 1)	7
Total params: 19132; trainable params: 19132		

4.3 Synergistic effects analysis of multiple parameters

A detailed analysis is conducted on the relationship between the design parameters and energy output of CDEG, utilizing the DNN model. During the analysis, the fixed parameters are set to default values, where f is 5 Hz, m_r is 0.049 kg, k_s is 100 N/m, λ_p is 3, U_{in} is 3000 V, the radii of the CDEG's top and bottom surfaces are respectively set at 0.02 and 0.06 m, meaning $\omega = 0.333$. To better evaluate the impact of each parameter on the output power, the following formula is used to express the main effect SS of the parameter within the selected parameter range:

$$SS = \sum_{i=1}^{k} \frac{(\bar{y}_i - \bar{y})^2}{n_i(k-1)}, \tag{30}$$

where k represents the number of groups, $\bar{y}_i$ denotes the mean value of the i^{th} group, $\bar{y}$ is the mean value of all samples, and n_i indicates the sample size of the i^{th} group.

Figure 15 displays the synergistic effects of varying the input voltage U_{in} with another varied parameter on the output energy, when the rest parameters are fixed to be the default values as set above. It can be observed that the SS for voltage U_{in} is generally larger than those of other parameters, slightly lower than the SS of excitation frequency. Additionally, there is a positive correlation between voltage and output power, indicating that voltage is the most influential parameter affecting the energy output of the CDEG. If the input voltage remains below the breakdown voltage of DE, increasing the input voltage can result in higher energy output. Figure 16 illustrates the synergistic effects of the radius ratio ω with another varied parameter on the output energy, and the rest parameters are fixed to be the default

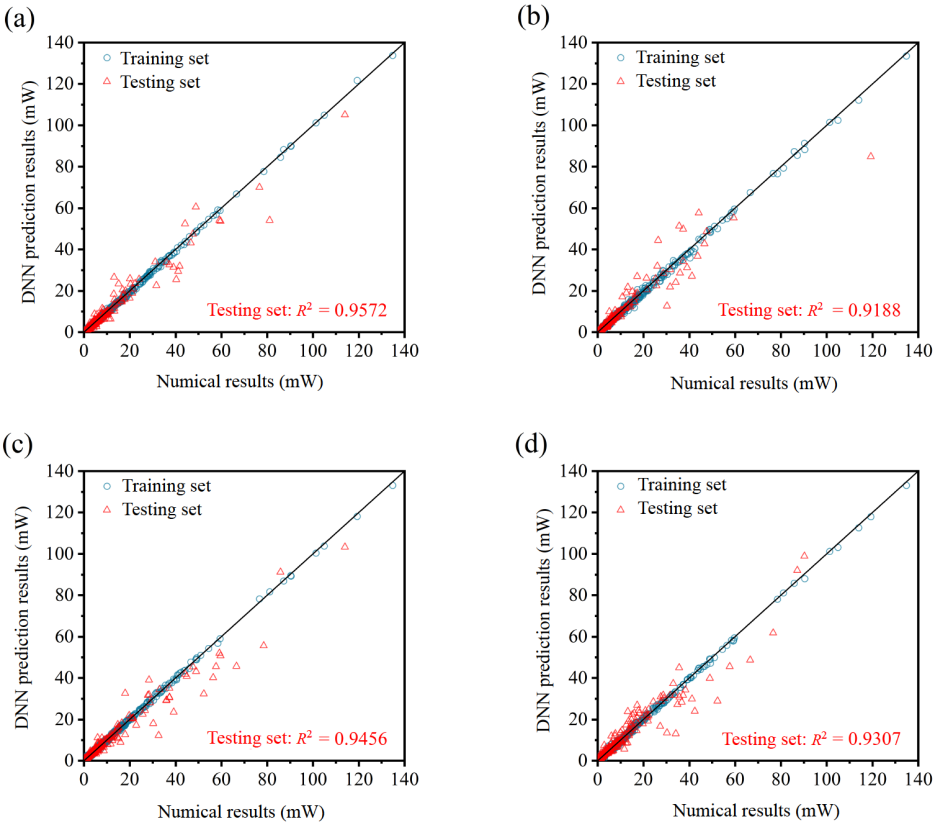

Figure 14 Comparison of the training results of output power for cross-validation: (a) Group I; (b) Group II; (c) Group III; (d) Group IV.

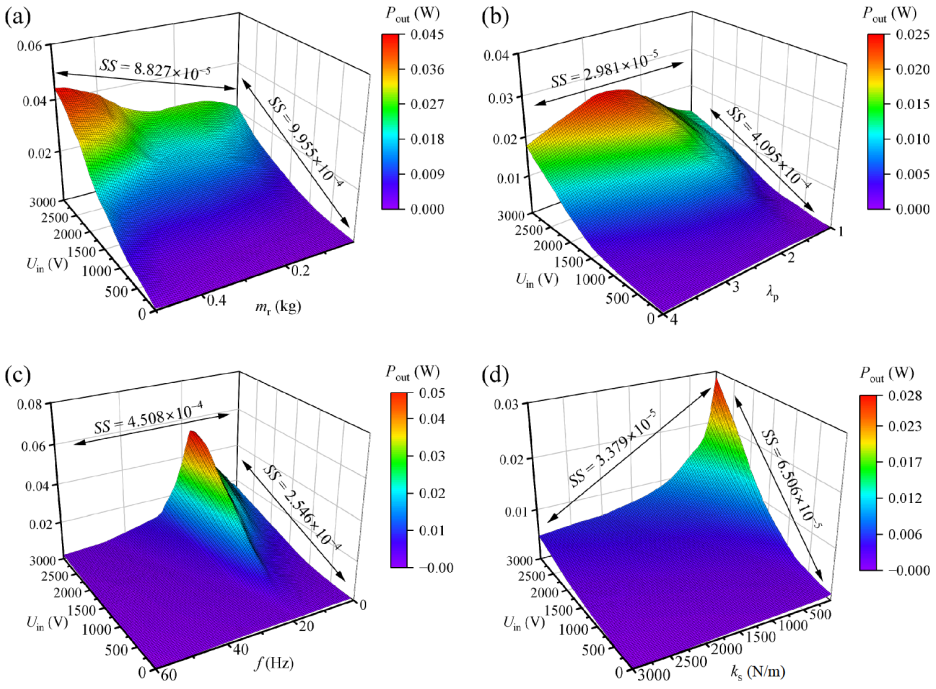

Figure 15 Influence of U_{in} and various parameters on output power of CDEGs: (a) equivalent mass; (b) pre-stretch ratio; (c) excitation frequency; (d) spring stiffness.

values. It is evident that the *SS* for *w* is substantially smaller compared to the *SS* of other parameters, suggesting that *w* has a relatively minor influence on the energy harvesting performance.

Figure 17 illustrates the mutual influence of equivalent mass, excitation frequency, spring stiffness, and pre-stretch ratio on the energy output of the CDEGs, when the remaining parameters are fixed at the default values. Figure 17(a) indicates that a reduction in m_r reduces the excitation frequency at which maximum energy output occurs. Figure 17(b), (d), and (e) reveals that energy output efficiency remains high for spring stiffness below 200 N/m, attributable to the greater deformations induced by lower stiffness springs, which amplifies the structural capacitance changes. However, due to the stress-softening phenomenon in DE during elongation, we set the minimum spring stiffness at

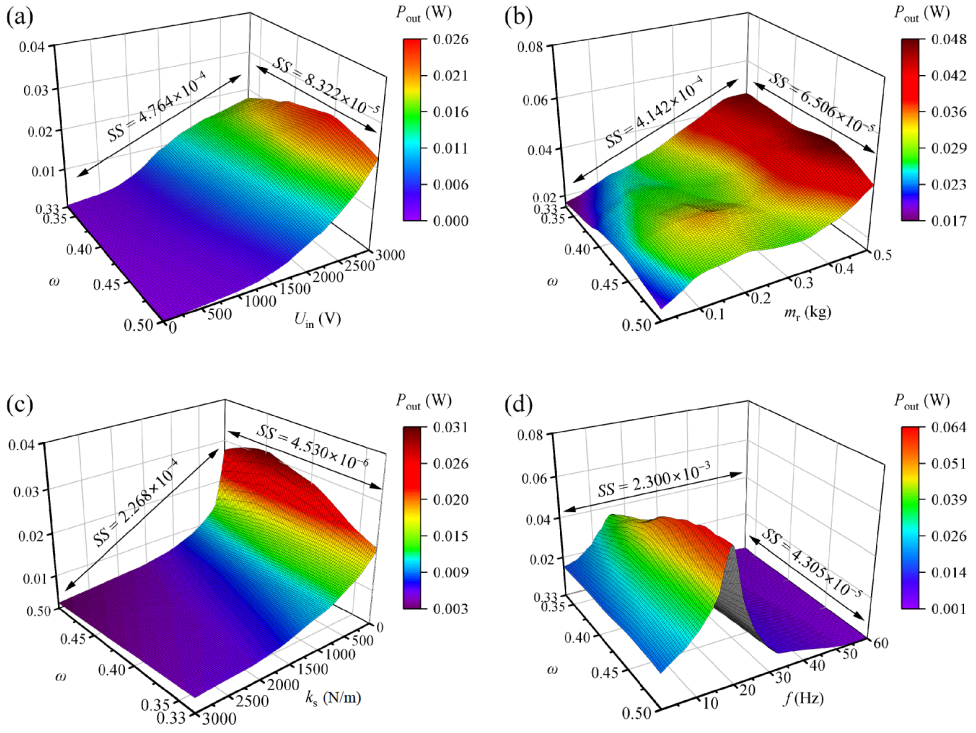

Figure 16 Influence of ω and various parameters on output power of CDEGs: (a) input voltage; (b) equivalent mass; (c) spring stiffness; (d) excitation frequency.

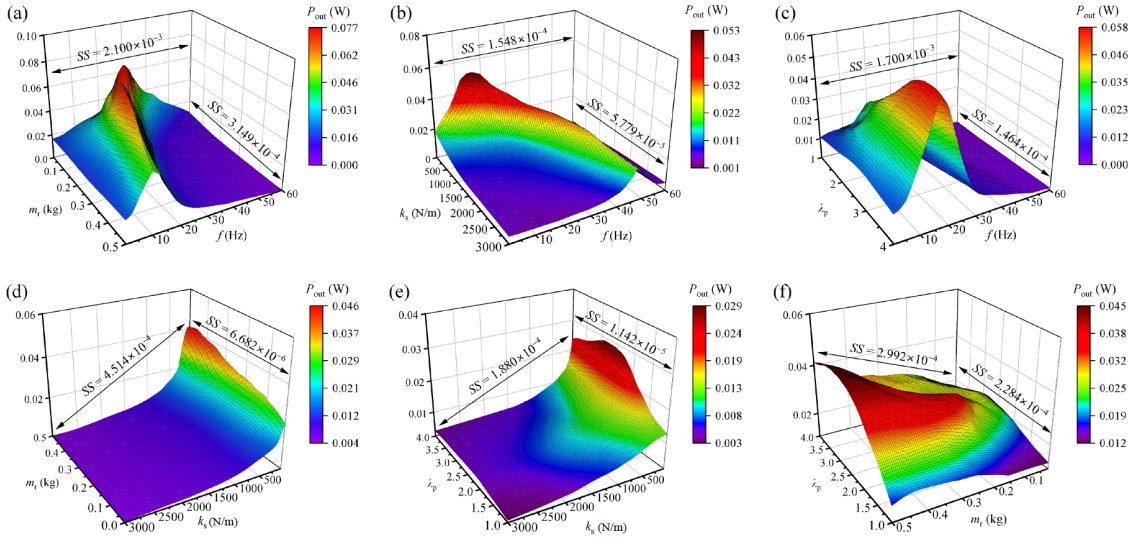

Figure 17 Influence of various on the output power of CDEGs: (a) equivalent mass and frequency; (b) spring stiffness and frequency; (c) pre-stretch ratio and frequency; (d) equivalent mass and spring stiffness; (e) pre-stretch ratio and spring stiffness; (f) pre-stretch ratio and equivalent mass.

50 N/m to ensure the film conforms to model assumptions. Figure 17(a)-(c) demonstrates that there exists an optimal excitation frequency for maximizing the energy output of CDEGs. Figure 17(c), (e), and (f) shows that the pre-stretch ratio between 2 and 3.5 can moderately enhance energy collection efficiency, primarily because DE is a hyperelastic material. A larger stretch ratio induces the DE material to enter a hardening phase, increasing material strength but hindering deformation, while a smaller pre-stretch ratio results in a thicker DE film, leading to smaller capacitance changes from deformation. In summary, voltage U_{in} has the most significant impact on the model's output capability, followed by excitation frequency f, equivalent mass m_r, and stiffness, which influence the output performance by controlling the model's resonance and resonance range. The pre-stretch ratio has a moderate effect on the output performance, with an optimal selection range existing. In contrast, the radius ratio w has a relatively minor influence.

5. Parameter optimization design and experimental validation of CDEGs

The issue of time costs in solving theoretical models impedes the optimization design of CDEG. However, the optimization method based on combining DNN and genetic algorithm can significantly reduce computational resources, due to the fast prediction ability of the developed DNN model. Hence, an NSGA-II framework is developed and receives the optimization objective functions based on the DNN model.

5.1 Multi-objective optimization and optimal design parameters

The influence of various parameters on the efficiency of the CDEG is complicated. It is difficult to select the optimal design parameters based solely on the parameter analysis from the previous section. Moreover, CDEGs generally operate in low-frequency vibrational environments, for instance, wave vibration typically below 2 Hz [50]; human motion frequency below 5 Hz; some vertical movements of the vehicles around 1 to 20 Hz and significant vibrations in structures and industrial equipment is approximately between 5 and 12 Hz. Therefore, CDEG requires the formulation of an optimization problem aimed at achieving sufficiently high energy harvesting efficiency at lower frequencies. This can be represented as follows:

$$\begin{cases} \max\ P_{out}(x_i), \\ \min\ x_3, \\ \text{s.t.}\quad u_i \geq x_i \geq l_i,\ i = 1,2,...,6, \end{cases} \tag{31}$$

where x_i represent the six design variables, u_i and l_i indicate the upper and lower bounds for each design variable, where the upper limit of input voltage and λ_p are 2000 V and 3, and ranges for other parameters are detailed in Table 2.

In this part, the NSGA-II algorithm coded by the Geatpy package in Python is employed for multi-objective optimization. The algorithm is configured with a population size of 500, a mutation probability of 0.2, a crossover probability of 0.9, and an evolutionary generation count of 3000. The resulting Pareto front is illustrated in Fig. 18. It is noted that the Pareto frontier provides the designer with many solutions, and any point in the Pareto frontier can be a solution.

5.2 Experimental validation of the optimization results

We selected a set of optimal solutions for experimental validation of the Pareto front diagram obtained in the previous section. The structural parameters and predicted outputs are presented in Table 4. It should be specially illustrated that the small differences between the experiment and optimization parameters lie in the reality test condition. The experimental device, established based on the parameters after optimization, is illustrated in Fig. 19(a). The apparatus is tested (Supplementary Video 1) for capacitance values at varying compressions, output voltage as time variations, and position of rigid block as time changes, as illustrated in Fig. 19(b)-(d). The actual output power is calculated to be 3.57 mW, which is close to the optimized result of 3.88 mW.

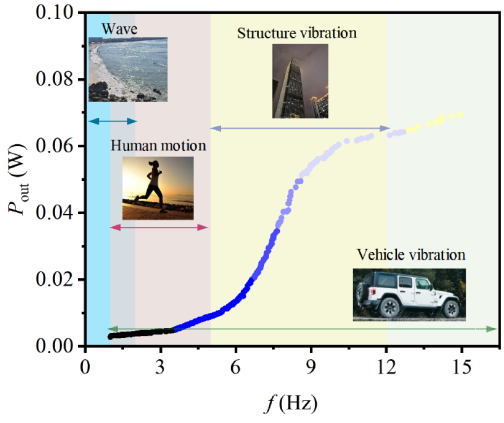

Figure 18 Pareto frontier of the excitation frequencies and energy output design optimization.

Table 4 Comparison of optimization and experiment parameters

Parameters	Optimization	Experiment
Input voltage U_{in} (V)	1993.117	2000
Pre-stretch ratio λ_p	2.98	3
Excitation frequency f (Hz)	2.21	2.21
Spring stiffness k_s (N/m)	48.5	50
Equivalent mass m_r (kg)	0.0466	0.046
The ratio of inner to outer diameter ω	0.338	0.333
Output power P_{out} (mW)	3.88	3.57

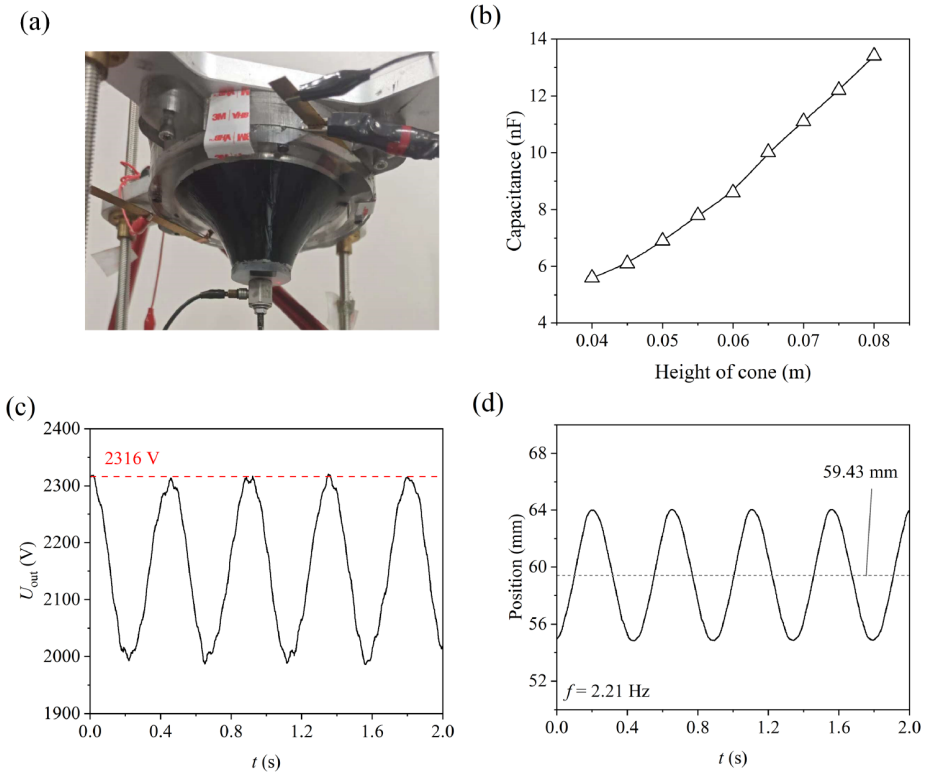

Figure 19 Experimental of CDEG after optimization: (a) the experimental apparatus established using the optimal parameters; (b) capacitance values of the CDEG under different deformation conditions; (c) variations in output voltage waveforms; (d) position-time history curve.

6. Conclusions

This study develops the FVP model of DE material considering deformation-dependent electrostriction and nonlinear viscoelasticity, whose parameters are fitted from experimental data. Experiments are carried out to validate the dynamic model and energy harvest theory. A DNN is employed to establish the relationship between six design parameters of CDEG and output energy. And then the CDEG for harvesting low-frequency vibration energy is designed. For the CDEG, the dynamical governing equation and energy output prediction theory based on the FVP model align more closely with experimental results compared to the model neglecting stretch-dependent. The study investigates the effects of various parameters on the output performance of CDEGs. The results indicate that higher input voltages, a pre-stretch ratio within the range of 2 to 3.5, and a spring stiffness below 200 N/m significantly enhance the energy output of the CDEG. Subsequently, an optimization framework based on DNN is proposed to maximize energy output, minimize excitation frequency, and determine optimal structural parameters. Experimental validation using the optimized device demonstrates a close match between the results and the predictions derived from the proposed optimization method. Based on this framework, the optimized CDEG model achieves maximum energy output power design within the frequency range of 1 to 16 Hz. Our study provides a deep understanding of the mechanism of the CDEG. Actually, the developed models CDEG can also be used for the practical design of other DE energy harvesting.

Appendix A

The uniaxial tensile experiments and capacitance testing experiments are carried out to calibrate the mechanical and electrical parameters of DE, which is VHB 4910 produced by 3M corporation in this paper.

A1. Mechanical parameter identification

The mechanical parameters C_i (i = 1, 2, 3), α, η, and electromechanical coupling parameters c_i (i = 1, 2, 3) in Eqs. (4) and (5) are measured in different experiments due to the assumption that the viscous part of the stress is independent of the electric field. Uniaxial tensile experiments at different rates are adopted to calibrate the hyperelastic C_i (i = 1, 2, 3) and viscous parameters α, η, and the dielectric constant tests of circular films under biaxial tensile are used to calibrate the electromechanical coupling parameters c_i (i = 1, 2, 3). Based on the uniaxial tensile and incompressible conditions, the stretch ratio of the specimen is assumed to be $\lambda_1 = \lambda$, $\lambda_2 = \lambda^{-1/2}$, $\lambda_3 = \lambda^{-1/2}$. In the absence of an electric field, the

nominal stress tensor can be given by

$$\mathbf{s} = \mathbf{F}^{-1}(\boldsymbol{\sigma}_{\mathrm{h}} + \boldsymbol{\sigma}_{\mathrm{v}}) = \frac{\partial w_{\mathrm{h}}}{\partial \mathbf{F}}\mathbf{F}^{\mathrm{T}} + 2\eta\mathbf{F}^{-1}\mathbf{D}^{\{\alpha\}}, \tag{A1}$$

by substituting Eqs. (4) and (9) into the preceding expression, the nominal stress along the tensile direction of the specimen under uniaxial tension can be represented as

$$s = 2\left[C_1 + 2C_2(\lambda^2 + 2\lambda^{-1} - 3) + 3C_3(\lambda^2 + 2\lambda^{-1} - 3)^2\right] \cdot (\lambda^2 - \lambda^{-1}) + 2\eta\frac{\lambda^{-1}}{\Gamma(1-\alpha)} \cdot \int_0^t (t-\tau)^{-\alpha}\lambda^{-3}(\tau)\cdot\lambda^2(t)\cdot\dot{\lambda}\mathrm{d}\tau. \tag{A2}$$

The uniaxial tensile experiments are carried out on the tensile testing machine. The sample is a rectangular DE film with length 5 cm and width 3 cm, as shown in Fig. A1(a). The short side of the specimen is fixed to test the force displacement curve in different stretching rates ($\dot{\lambda}$ = 0.0167, 0.0500, 0.0833, 0.1167, 0.1500, 0.1833 s^{-1}), and repeats three times. The stretching rate $\dot{\lambda}$ = 0.0167 s^{-1} is regarded as quasi-static loading rate. The mechanical parameters can be derived by fitting experimental data based on Eq. (A2).

As shown in Fig. A1(b), the hyperelastic model parameters are fitted using quasi-static tensile data, resulting in C_1 = 14.30 kPa, C_2 = −0.520 kPa, and C_3 = 0.016 kPa. Subsequently, by combining the hyperelastic model data with loading data at various rates, viscoelastic model parameters with a high degree of matching are determined to be α = 0.37 and η = 50000 Pa. The calibrated model demonstrates a good fit with the experimental data.

A2. Electromechanical coupling parameters identification

The dielectric constant testing utilizes circular film specimens, where the circular DE membrane is subjected to equal-order biaxial tension in the plane. An electric field is applied in the thickness direction, and its stretch ratio is assumed to be $\lambda_1 = \lambda^{-1/2}$, $\lambda_2 = \lambda^{-1/2}$, $\lambda_3 = \lambda$, and the electric field is **E**. The spatial polarization vector **P** is obtained from the polarization-based lumped parameter model and basic definition as follows [37]:

$$\mathbf{P} = -\mathbf{F}\frac{\partial w_{\mathrm{e}}}{\partial \widetilde{\mathbf{E}}}, \tag{A3}$$

$$\mathbf{P} = \varepsilon_0(\varepsilon_{\mathrm{r}} - 1)\mathbf{E}, \tag{A4}$$

where ε_0 is the permittivity of vacuum, and ε_{r} is the relative dielectric constant.

Compare Eqs. (A3) and (A4), the expression of the relative permittivity can be obtained as

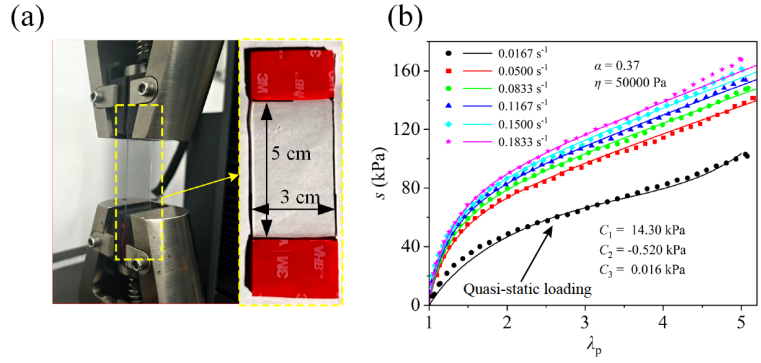

Figure A1 Mechanical parameters calibration: (a) uniaxial tensile test; (b) the fitting curve based on Eq. (A2).

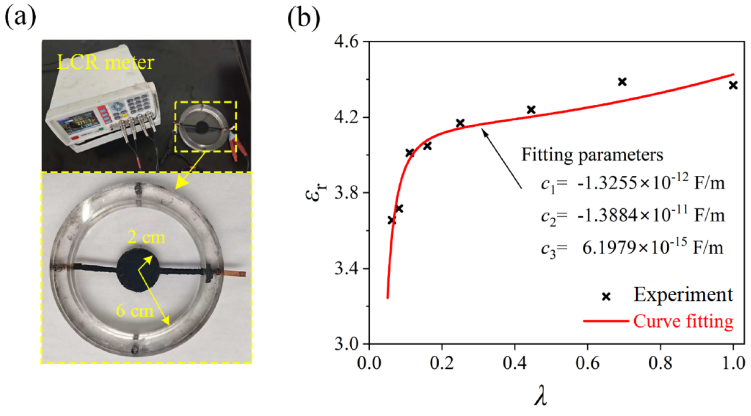

Figure A2 Electrical parameters calibration: (a) relative dielectric constant test; (b) the fitting curve based on Eq. (A5).

$$\varepsilon_{\mathrm{r}} = 1 - \frac{2c_1}{\varepsilon_0}\lambda^2 - \frac{2c_2}{\varepsilon_0} - \frac{2c_3}{\varepsilon_0}\lambda^{-2}. \tag{A5}$$

The test samples are carried out by stretching the circular films with different radius to the same size, the stretch ratios used in this paper are λ = 1.0000, 0.6940, 0.4444, 0.2500, 0.1600, 0.1111, 0.0816, 0.0625, and the same circular regions (radius is 2 cm) in the middle are selected to paste flexible electrodes (MG Chemicals 846 Carbon Conductive Grease), show in Fig. A2(a). The relative permittivity of circular films with different stretch rates is tested, and material parameters of the electric part are obtained by fitting according to Eq. (A5).

Figure A2(b) presents the results of dielectric constant tests and their corresponding fitting curve. The relative permittivity ε_{r} of VHB 4910 obtained in the experiment is 4.37 when λ = 1, and the relative permittivity decreases to 3.65 with λ = 0.0625, which is a relative decrease of 16.47%. The electrical model parameters obtained by fitting the experimental data are $c_1 = -1.3255\times10^{-12}$ F/m, $c_2 = -1.3884\times10^{-11}$ F/m, and $c_3 = 6.1979\times10^{-15}$ F/m. The fitting curves are in good agreement with the experimental data.

Conflict of interest *On behalf of all authors, the corresponding author states that there is no conflict of interest.*

Author contributions *Demin Zhao wrote the paper, made the theoretical derivation and numerical calculation, and provided the funding support. Aoyu Xiao made some of the numerical calculations, designed and carried out all the experiments, analyzed experimental data, and wrote some of the paper. Zewen Gu analyzed the DNN. Menghang Chen carried out the experiments. Guoqiang Xu provided the experimental apparatus. Jianlin Liu revised the paper. Bin Zhao carried out some of the experiments and provided the project administration.*

Acknowledgements *This work was supported by the National Natural Science Foundation of China (Grant Nos. 12372027 and 12402109), the Natural Science Foundation of Shandong Province (Grant No. ZR2022MA086), and the Basic Scientific Research Expenses of Central Government Universities (Grant No. 23CX03010A).*

1 H. Wu, Y. A. Huang, F. Xu, Y. Duan, and Z. Yin, Energy harvesters for wearable and stretchable electronics: From flexibility to stretchability, Adv. Mater. **28**, 9881 (2016).
2 J. Zhou, H. Tang, L. Zeng, Z. Zhang, J. Zhao, A. Li, L. Kong, M. Tang, and Y. Hu, A self-powered and self-sensing wave energy harvesting system for the sea-crossing bridge, Mater. Today Nano **27**, 100500 (2024).
3 X. Du, L. Du, P. Li, X. Liu, Y. Han, H. Yu, K. Tao, and L. Tang, A dielectric elastomer and electret hybrid ocean wave power generator with oscillating water column, Nano Energy **111**, 108417 (2023).
4 D. Yan, D. Tao, D. Xu, Y. Sun, B. Deng, G. Cao, J. Fang, and W. Xu, Flexible arc-shaped triboelectric nanogenerator for all directions and highly efficient biomechanical energy harvesting and human motion monitoring, Nano Energy **129**, 110000 (2024).
5 K. Ichikawa, and W. Hijikata, Energy harvesting from biting force with thin sheet harvester based on electret and dielectric elastomer, Nano Energy **99**, 107357 (2022).
6 I. Al-Najati, K. W. Chan, A. F. Jasim, and S. Y. Pung, Development and optimization of a new end-cap tire-strain piezoelectric energy harvester (TSPEH), Energy Convers. Manage. **303**, 118109 (2024).
7 B. Zhang, Z. Zhao, Y. Li, X. Zhang, X. Li, D. Hao, and Z. Zhang, Design and analysis of a piezoelectric energy harvesting shock absorber for light truck applications, Appl. Energy **377**, 124569 (2025).
8 L. Peng, Y. Wang, Y. Qi, X. Ru, and X. Hu, A hybrid piezoelectric-electromagnetic energy harvester used for harvesting and detecting on the road, J. Clean. Prod. **426**, 139052 (2023).
9 Z. Zhou, H. Huang, D. Cao, W. Qin, P. Zhu, and W. Du, Harvest more bridge vibration energy by nonlinear multi-stable piezomagnetoelastic harvester, J. Phys. D-Appl. Phys. **57**, 135501 (2024).
10 Z. Xu, J. Tan, H. Chen, K. Di, K. Bao, J. Cheng, X. Xie, S. Zheng, S. Lin, J. Cai, T. Cheng, L. Liu, Z. L. Wang, and S. E, Fatigue-resistant high-performance dielectric elastomer generator in alternating current method, Nano Energy **109**, 108314 (2023).
11 H. Yu, Z. Hao, X. Liu, Q. Feng, P. Li, K. Tao, and X. Du, Ocean wave energy harvesting: Utilizing buoy float to induce dielectric elastomer deformation and electret vibration for power generation, Nano Energy **131**, 110192 (2024).
12 H. J. Ko, H. Seong, and J. Kim, Stacked triboelectric nanogenerator with grating structures for harvesting vertical motion, Nano Energy **131**, 110258 (2024).
13 L. Zhang, H. Zheng, B. Liu, Q. Liang, K. Li, J. Liu, and W. Chen, A piezoelectric energy harvester for multi-type environments, Energy **305**, 132218 (2024).
14 B. Chu, X. Zhou, K. Ren, B. Neese, M. Lin, Q. Wang, F. Bauer, and Q. M. Zhang, A dielectric polymer with high electric energy density and fast discharge speed, Science **313**, 334 (2006).
15 T. G. McKay, B. M. O'Brien, E. P. Calius, and I. A. Anderson, Soft generators using dielectric elastomers, Appl. Phys. Lett. **98**, 142903 (2011).
16 S. Yang, X. Zhao, and P. Sharma, Avoiding the pull-in instability of a dielectric elastomer film and the potential for increased actuation and energy harvesting, Soft Matter **13**, 4552 (2017).
17 T. Q. Lu, and Z. G. Suo, Large conversion of energy in dielectric elastomers by electromechanical phase transition, Acta Mech. Sin. **28**, 1106 (2012).
18 S. J. A. Koh, X. Zhao, and Z. Suo, Maximal energy that can be converted by a dielectric elastomer generator, Appl. Phys. Lett. **94**, 262902 (2009).
19 Z. H. Lai, J. L. Wang, C. L. Zhang, G. Q. Zhang, and D. Yurchenko, Harvest wind energy from a vibro-impact DEG embedded into a bluff body, Energy Convers. Manage. **199**, 111993 (2019).
20 C. L. Zhang, Z. H. Lai, M. Q. Li, and D. Yurchenko, Wind energy harvesting from a conventional turbine structure with an embedded vibro-impact dielectric elastomer generator, J. Sound Vib. **487**, 115616 (2020).
21 X. Xie, S. Zheng, J. Tan, J. Cheng, J. Cai, Z. Xu, and Z. Shiju E, An integrated charge excitation alternative current dielectric elastomer generator for joint motion energy harvesting, Adv. Mater. Technol. **9**, 2301172 (2024).
22 T. Hanuhov, R. Brighenti, and N. Cohen, Energy harvesting with dielectric elastomer tubes: Active and (responsive materials-based) passive approaches, Smart Mater. Struct. **33**, 055004 (2024).
23 J. W. Zhang, S. M. Ding, and H. F. Wu, Dynamics and energy harvesting performance of a nonlinear arc-cylinder type dielectric elastomer oscillator under unidirectional harmonic excitations, Int. J. Mech. Sci. **244**, 108090 (2023).
24 G. Y. Gu, U. Gupta, J. Zhu, L. M. Zhu, and X. Zhu, Modeling of viscoelastic electromechanical behavior in a soft dielectric elastomer actuator, IEEE Trans. Robot. **33**, 1263 (2017).
25 Y. Chen, G. Kang, J. Yuan, and T. Li, Experimental study on pure-shear-like cyclic deformation of VHB 4910 dielectric elastomer, J. Polym. Res. **26**, 186 (2019).
26 R. K. Sahu, and K. Patra, Rate-dependent mechanical behavior of VHB 4910 elastomer, Mech. Adv. Mater. Struct. **23**, 170 (2015).
27 X. Zhao, and Z. Suo, Electrostriction in elastic dielectrics undergoing large deformation, J. Appl. Phys. **104**, 123530 (2008).
28 X. Xing, L. Chen, C. Zhao, and S. Yang, Modulation of the dynamic response and stability of dielectric balloon by stretch-dependent

dielectric permittivity, J. Appl. Phys. **134**, 104101 (2023).
29 L. Liu, Y. Han, and H. Yong, Bulging of dielectric elastomer tubes considering residual stress and viscoelasticity, Int. J. Mech. Sci. **267**, 108955 (2024).
30 A. Khurana, A. Kumar, S. K. Raut, A. K. Sharma, and M. M. Joglekar, Effect of viscoelasticity on the nonlinear dynamic behavior of dielectric elastomer minimum energy structures, Int. J. Solids Struct. **208-209**, 141 (2021).
31 Y. Li, I. Oh, J. Chen, H. Zhang, and Y. Hu, Nonlinear dynamic analysis and active control of visco-hyperelastic dielectric elastomer membrane, Int. J. Solids Struct. **152-153**, 28 (2018).
32 T. Karner, R. Belšak, and J. Gotlih, Using a fully fractional generalised Maxwell model for describing the time dependent sinusoidal creep of a dielectric elastomer actuator, Fractal Fract. **6**, 720 (2022).
33 Q. Li, and Z. Sun, Dynamic modeling and response analysis of dielectric elastomer incorporating fractional viscoelasticity and gent function, Fractal Fract. **7**, 786 (2023).
34 M. Wissler, and E. Mazza, Electromechanical coupling in dielectric elastomer actuators, Sens. Actuat. A-Phys. **138**, 384 (2007).
35 B. Li, H. Chen, J. Qiang, and J. Zhou, A model for conditional polarization of the actuation enhancement of a dielectric elastomer, Soft Matter **8**, 311 (2012).
36 S. M. A. Jiménez, and R. M. McMeeking, Deformation dependent dielectric permittivity and its effect on actuator performance and stability, Int. J. Non-Linear Mech. **57**, 183 (2013).
37 T. Schlögl, and S. Leyendecker, A polarisation based approach to model the strain dependent permittivity of dielectric elastomers, Sens. Actuat. A-Phys. **267**, 156 (2017).
38 A. Kumar, and K. Patra, Proposal of a generic constitutive model for deformation-dependent dielectric constant of dielectric elastomers, Eng. Sci. Tech. Int. J. **24**, 1347 (2021).
39 X. Xing, L. Chen, C. Zhao, and S. Yang, Nonlinear oscillations of dielectric elastomer actuators with stretch-dependent permittivity, J. Appl. Mech. **89**, 111009 (2022).
40 A. Haroun, and C. Lee, Dielectric-elastomer-enhanced triboelectric nanogenerator with amplified outputs, Sens. Actuat. A-Phys. **333**, 113270 (2022).
41 Y. Jiang, S. Liu, M. Zhong, L. Zhang, N. Ning, and M. Tian, Optimizing energy harvesting performance of cone dielectric elastomer generator based on VHB elastomer, Nano Energy **71**, 104606 (2020).
42 L. Li, J. Li, L. Qin, J. Cao, M. S. Kankanhalli, and J. Zhu, Deep reinforcement learning in soft viscoelastic actuator of dielectric elastomer, IEEE Robot. Autom. Lett. **4**, 2094 (2019).
43 N. Wang, H. Guo, B. Chen, C. Cui, and X. Zhang, Design of dielectric elastomer actuator using topology optimization method based on genetic algorithm, Smart Mater. Struct. **28**, 065013 (2019).
44 J. Ma, T. Y. Zhang, and S. Sun, Machine learning-assisted shape morphing design for soft smart beam, Int. J. Mech. Sci. **267**, 108957 (2024).
45 A. L. Li, P. Cuvin, S. Lee, J. Gu, C. Tugui, and M. Duduta, Data-driven long-term energy efficiency prediction of dielectric elastomer artificial muscles, Adv. Funct. Mater. **34**, 2406710 (2024).
46 A. Dorfmann, and R. W. Ogden, Nonlinear electroelasticity, Acta Mech. **174**, 167 (2005).
47 M. Wissler, and E. Mazza, Modeling of a pre-strained circular actuator made of dielectric elastomers, Sens. Actuat. A-Phys. **120**, 184 (2005).
48 D. M. Zhao, Y. D. Yin, and J. L. Liu, A fractional finite strain viscoelastic model of dielectric elastomer, Appl. Math. Model. **100**, 564 (2021).
49 Z. Gu, Y. Liu, D. J. Hughes, J. Ye, and X. Hou, A parametric study of adhesive bonded joints with composite material using black-box and grey-box machine learning methods: Deep neuron networks and genetic programming, Compos. Part B-Eng. **217**, 108894 (2021).
50 A. Azam, A. Ahmed, H. Li, A. M. Tairab, C. Jia, N. Li, and Z. Zhang, Design and analysis of the optimal spinning top-shaped buoy for wave energy harvesting in low energy density seas for sustainable marine aquaculture, Ocean Eng. **255**, 111434 (2022).

基于深度学习的锥形介电能量收集器高效优化方法

赵德敏, 肖奥宇, 谷泽文, 陈梦航, 徐国强, 赵斌, 刘建林

摘要 介电弹性体(DE)是一种电活性聚合物, 具有高能量输出、柔韧、轻质、优异的机械顺应性和低成本等特点, 特别适用于制作能量收集器. 能量收集效率是评估能量收集器性能的关键指标, 其取决于结构配置以及DE材料的机械和介电特性. 本文通过结合分数阶黏弹性模型和基于极化的集总参数模型, 提出了一种分数阶黏弹性极化(FVP)模型. 建立了考虑拉伸依赖电致伸缩和非线性黏弹性的锥形介电能量发生器(CDEG)动力学模型. 此外, 开发了一种深度神经网络(DNN)模型, 以探索各种参数与CDEGs输出能量之间的关系, 从而高效、准确地预测CDEGs的能量输出. 基于DNN模型, 采用非支配排序遗传算法Ⅱ(NSGA-Ⅱ)获得了CDEGs的优化参数设计. 实验验证了FVP模型能够准确预测CDEG的输出能量, 且所建立的优化设计框架能够精确提供CDEG的最佳设计参数, 为高效介电能量发生器的设计和制造提供了帮助.